A GENUINELY MULTIDISCIPLINARY JOURNAL

CHEMPLUSCHEM

CENTERING ON CHEMISTRY

Accepted Article

Title: Hierarchical porous NiO/β-NiMoO4 heterostrucutre as superior anode material for lithium storage

Authors: Zhijian Wang, Shilin Zhang, Hai Zeng, Haimin Zhao, Wei Sun, Meng Jiang, Chuanqi Feng, Jianwen Liu, Tengfei Zhou, Yang Zheng, and Zaiping Guo

To be cited as: *ChemPlusChem* 10.1002/cplu.201800220

Link to VoR: http://dx.doi.org/10.1002/cplu.201800220

A Journal of ChemPubSoc Europe

WILEY-VCH www.chempluschem.org

10.1002/cplu.201800220

Hierarchical porous NiO/β-$NiMoO_4$ heterostructure as superior anode material for lithium storage

Zhijian Wang[1†], Shilin Zhang[2†], Hai Zeng[3], Haimin Zhao[4], Wei Sun[4], Meng Jiang[1], Chuanqi Feng[1], Jianwen Liu[1], Tengfei Zhou[2,3,5], Yang Zheng[2*], Zaiping Guo[1, 2*]

[1] *Hubei Collaborative Innovation Centre for Advanced Organic Chemical Materials, Ministry of Education Key Laboratory for Synthesis and Applications of Organic Functional Molecules, Hubei University, Wuhan 430062, China.*
[2] *Institute for Superconducting and Electronic Materials, School of Mechanical, Materials, and Mechatronics Engineering, University of Wollongong, North Wollongong, NSW 2500, Australia*
[3] *Key Laboratory of Catalysis and Materials Science of the State Ethnic Affairs Commission & Ministry of Education, South-Central University for Nationalities, Wuhan, 430074, P. R. China*
[4] *Tianneng Battery Group Co. Ltd, 18 Baoqiao Road, Huaxi Industrial Functional zone, Changxing, Zhejiang, 313100, China*
[5] *Key Laboratory of Advanced Energy Materials Chemistry (Ministry of Education), Nankai University, Tianjin 300071, China*

*Corresponding author: zguo@uow.edu.au; yz966@uowmail.edu.au

ABSTRACT

Ternary transition metal oxides (TTMOs) have attracted considerable attention for rechargeable batteries because of its fascinating properties. However, the unsatisfied electrochemical performance originating from the poor intrinsic electronic conductivity and inferior structural stability impede their practical applications. In this work, the novel hierarchical porous NiO/β-$NiMoO_4$ heterostructure has been fabricated and exhibited high reversible capacity, superior rate capability, and excellent cycling stability towards LIBs, which is much better than the corresponding single phase $NiMoO_4$ and NiO materials. The significantly enhanced electrochemical properties can be attributed to its superior structural characteristics, including the large surface area, abundant pores, fast charge transfer, and catalytic effect of the intermediate product of metallic nickel. The NiO/β-$NiMoO_4$ heterostructure delivered a high capacity of 1314 mA h g^{-1} at 0.2 A g^{-1} after 100 cycles. Furthermore, even after 400 cycles at 1 A g^{-1}, the reversible capacity still remained at around 500 mA h g^{-1}. These results indicate that the NiO/β-$NiMoO_4$ heterostructure shows great potential as anode materials for high-performance LIBs.

Keywords：*Ternary transition metal oxides, heterostructure, β-$NiMoO_4$, NiO, Li-ion batteries*

Introduction

High-performance rechargeable lithium-ion batteries (LIBs) are gradually becoming indispensable units in portable commercialized electronics, electric vehicles, and renewable energy storage.[1,2] Nevertheless, the conventional LIBs based on the prevailing carbon-based intercalation materials are already reaching their energy capacity limits. Hence, tremendous efforts have been devoted to exploring novel anode materials with higher energy density, sustainable lifespan, cost-effectiveness, and safe working potential to make these materials applicable for the advanced LIBs to meet the ever-growing demands for electrical applications.[3–5]

Ternary transition metal oxides (TTMOs) are emerging as promising candidate electrode materials for high-energy LIBs due to their distinctive properties.[6,7] It is widely demonstrated that TTMOs generally exhibit superior reversible capacity, good structural stability, and high electronic conductivity. Specifically, the synergetic effects associated with their complex chemical compositions typically contribute to remarkable electrochemical activities and high specific capacity, while the multiple valences of the cations are beneficial to achieve more versatile redox reactions.[8,9] More importantly, because of the lower activation energy for electron transfer between different cations, it normally possess higher electrical conductivity than their corresponding binary metal oxide counterparts.[10] Among various potential TTMOs, spinel structure nickel molybdate ($NiMoO_4$) has been regarded as an attractive material in view of its high theoretical capacity (about 984 mA h g^{-1}), good electrical conductivity, environmental friendliness, and low cost.[11,12] At atmospheric pressure,

there are two phases of $NiMoO_4$ both with monoclinic structure: the α-$NiMoO_4$ (low temperature stable phase) and β-$NiMoO_4$ (high temperature stable phase). The most obvious difference between those two polymorphs is the coordination of the Mo^{6+} ions, with pseudo-octahedral coordination in the α-$NiMoO_4$ phase and distorted tetrahedral coordination in the β-$NiMoO_4$ phase.[13] Generally, β-$NiMoO_4$ has higher intrinsic conductivity and reactivity than that of α-$NiMoO_4$,[14] but it is very difficult to be prepared and maintained. In addition, $NiMoO_4$ electrode materials suffer from some drawbacks, such as the huge volume change, low electrochemical reversibility, leading to inferior electrochemical performance.[15,16] Therefore, rational design and facile synthesis of β-$NiMoO_4$ materials for high energy LIBs still remains a significant challenge.

Constructing heterostructure by combining active materials with metal oxides or sulfides has proven to be an effective way to conquer above-mentioned obstacles.[17,18] It is believed that such constructed heterostructure usually enables abundant electrochemical active sites, short ion diffusion path, and good structural stability originating from the synergistic effect of different components, thus exhibiting better electrochemical performance.[19] For example, Yuan et.al, developed the hierarchical mesoporous ZnO/$ZnFe_2O_4$ sub-microcubes which exhibited better electrochemical Li-storage properties than the single-phase $ZnFe_2O_4$, owning to the striking synergistic effect between the bi-component active, well-dispersed ZnO and ZFO phases at the nanoscale.[20] Mai et al. found that hierarchical $MnMoO_4$/$CoMoO_4$ heterostructured nanowires shown enhanced specific capacitance and reversibility

when compared to the $MnMoO_4$ and $CoMoO_4$ electrodes.[21] Similarity, other hybrid heterostructures such as the $ZnCo_2O_4$/NiO core/shell nanowires,[22] NiO-Co_3O_4 nanoplates,[23] CoO/$CoFe_2O_4$ nanocomposites,[24] and $CoMoO_4$/Co_3O_4 composites,[25] have been employed as LIB electrodes and demonstrated improved reversible capacity and cycling performance.

Besides the favorable component, the structure also plays important roles in determining the electrochemical property of the developed electrode materials. It is considered that the hierarchical architecture constructed from 2D building blocks possess superior structural characteristics featuring in large specific surface area, more accessible pores, high structural stability, endowing them promising prospects for energy-related applications.[26] Undoubtedly, the large specific surface would provide rich Li storage active sites, while the generated numerous pores may offer additional space to accommodate the volume expansion, consequently maintaining the structural stability and electrode integrity. Lou et al, synthesized the hierarchical tubular structure of Co-Mn mixed metal oxides manifesting excellent electrochemical properties when employed as electrodes in Li-ion batteries and hybrid supercapacitors.[27] A hierarchical fascicular structure of Zn_2GeO_4 anode obtained through a wet chemistry method also exhibited remarkable Li-ion storage performance, since the hierarchical structure could alleviate the volume changes and retain the whole configuration, while the small building units will enlarge the contact area for electrode/electrolyte and construct the integrated interlaced conductive network.[28]

Herein, we have designed and constructed a novel hierarchical porous NiO/β-$NiMoO_4$ (NNMO) heterostructure via a facile hydrothermal technique followed by a calcination process. Interestingly, the NiO phases in the NNMO heterostructure could be regarded as a multifunctional layer, which can not only contribute to high theoretical capacity, but also function as the mechanical buffer to alleviate the huge volume changes of $NiMoO_4$ matrix, thus offering high capacity and good structural stability. Furthermore, the generated metallic nickel (Ni) nanoparticles from the lithiation reaction of NiO nanosheets with Li are able to promote the reversibly decompose of Li_2O during delithiation process, leading to high initial columbic efficiency and enhanced reversible capacity of the $NiMoO_4$, while the abundant pores produced from the surface interconnected nanosheets and the self-assembled microspheres with hierarchical structure will provide more space to relieve the induced-stress during lithiation/delithiation processes and preserve the structural integrity. As expected, the as-prepared NiO/β-$NiMoO_4$ heterostructured anode exhibited much better electrochemical Li storage properties than those of single-phase NiO or $NiMoO_4$ counterparts. Such significantly enhanced electrochemical performance can be attributed to its superior structural characteristics achieved by rational structure engineering of the electrode.

Results and discussion

The synthesis of hierarchical porous NiO/β-$NiMoO_4$ (NNMO) heterostructure by a novel and facile strategy is schematically illustrated in Scheme 1. First, appropriate

proportions of Ni^{2+} and MoO_4^{2-} precursors were homogeneously mixed into deionized water under magnetic stirring for certain time, so that the acetate could be adsorbed on the surface of MoO_4^{2-} by electrostatic interaction, and after that, the NNMO was obtained by oxidation of the as-prepared precursor mixture at 550 °C under oxygen atmosphere. For further comparison, single phase NiO (NO) and $NiMoO_4$ (NMO) were also fabricated by similar processes, with the exception of the different precursors that were chosen.

The purity and crystal structure of fabricated samples were analyzed by powder X-ray diffraction (XRD). The XRD patterns in Figure 1a confirm that the as-prepared NNMO materials are composed of pure β-phase $NiMoO_4$ (JCPDS Card No. 12-0348) and cubic bunsenite NiO (JCPDS Card No. 47-1049), indicating the coexistence of pure β-$NiMoO_4$ and NiO phase in the obtained NNMO composite. Furthermore, the formation of cubic NiO phase in the hybrid heterostructure is revealed by the diffraction peaks centered at 37.25°, 43.28°, and 62.89°, corresponding to the (111), (200), and (220) crystal planes, respectively. The remarkable diffraction peak at the value of 26.65° can be indexed to the characteristic (220) planes of β-$NiMoO_4$, suggesting the high purity of the β-phase $NiMoO_4$, without any trace/residual of the α-phase.[29] As shown in Figure S1a (Supporting Information), the diffraction patterns of prepared single-phase NO are well matched with pure NiO (JCPDS Card No. 47-1049), while all the diffraction peaks in Figure S1b (Supporting Information) can be assigned to the pure monoclinic α-$NiMoO_4$ (JCPDS Card No. 33-0948). Notably, no diffraction peaks can be indexed to β-phase $NiMoO_4$.

N_2 adsorption/desorption measurement were carried out to analyze the physical properties of the obtained samples (Figure 1b-1c). As presented in Figure 1b, the isotherm curves of all three samples show distinct type IV adsorption isotherm with H1-type hysteresis loops within a relative pressure P/P_0 range from 0.05 to 0.95 in the desorption isotherm, implying the existence of numerous pores. Based on the BET method analysis, it was found that the NNMO has a much larger specific surface area of 23.20 $m^2 g^{-1}$ with a total pore volume of 2.4 $cm^3 g^{-1}$, compared to the single-phase NO (10.45 $m^2 g^{-1}$) and NMO (18.40 $m^2 g^{-1}$) (Inset in Figure1b). Accordingly, the BJH pore size distribution profiles derived from the adsorption branches of isotherms were also calculated and are shown in Figure 1c. The pore size distribution curves for NNMO reveal that most of the pores range between 20 and 50 nm, markedly confirming the existence of a kind of mesoporous nanostructure. In addition, the narrow pore size distributions of NO and NMO show that the numerous pores are mainly macropores. Impressively, the unique structural features including the high specific surface area and abundant porous structure of NNMO heterostructure will not only provide many electroactive sites, large electrode/electrolyte contact area as well as easy access of electrolyte, but also accommodate the huge volume changes of the electrode during repeated lithiation/delithiation processes,[8,30,31] thus making it extremely beneficial to high-rate performance and long-cycle stability for Li ions storage.

The chemical states and elemental composition of the as-synthesized sample were further characterized by the X-ray photoelectron spectroscopy (XPS) technique.

As displayed in Figure 2a, the whole survey scan of the NNMO primarily demonstrates the presence of the elements Ni, Mo, and O. The high-resolution spectrum of Ni 2p (Figure 2b) can be deconvoluted into two main peaks by using the Gaussian fitting method, with the binding energies centered at 855.9 eV and 873.8 eV, corresponding to two spin-orbit doublets (Ni $2p_{3/2}$ and Ni $2p_{1/2}$) and two weak shake-up satellite peaks of nickel located at 861.5 eV and 880.1 eV, respectively.[32,33] The spin-energy separation of 17.9 eV is characteristic of the presence of Ni^{2+}.[34] On the other hand, the binding energies of Mo $3d_{5/2}$ and Mo $3d_{3/2}$ (Figure 2c) are located at 232.0 eV and 235.1 eV, respectively. The binding energies and the energy separation (3.1 eV) are characteristics of the Mo^{6+} oxidation state in $NiMoO_4$.[35] Figure 2d clearly shows the high-resolution spectrum in the O 1s region, which consists of a main peak located at 531.7 eV coupled with a shoulder at 532.7 eV. Therefore, the XPS results indicate the presence of both β-$NiMoO_4$ and NiO in the composite, which is consistent with the XRD result (Figure 1a).

The detailed morphology and microstructure of the as-prepared hierarchical porous NiO/β-$NiMoO_4$ heterostructure were investigated by the scanning electron microscopy (SEM) and high-resolution transmission electron microscopy (HRTEM). Figure 3a,b shows the representative SEM images of the NNMO at low and high magnification, respectively. It can be seen that the NNMO shows typical hierarchical porous microspheres, constructed from large amount of nanosheets with a thickness of 10~20 nm. Moreover, close observation can reveal that there are numerous nanopores generated on the nanosheets (Figure 3b) and the assembled nanosheets also formed

abundant large pores, which is also consistent with the BET results. The TEM images further confirm the hierarchical porous structure of the NNMO sample. (Figure 3c,d) These pores could promote the electrolyte to access the interior portion of material and offer enough additional space to accommodate the volume changes of the electrodes, thus improving electrochemical performance for Li-ion storage. Furthermore, the marked interplanar distances in the high resolution TEM image are 0.336 and 0.241 nm (Figure 3e), corresponding to the (220) and (111) lattice planes of β-$NiMoO_4$ and NiO, respectively, certifying the presence of the two phases in the composite. More interestingly, the β-$NiMoO_4$ and the NiO nanosheets are in tight contact with each other and form the heterostructure, which may promote rapid ion/electron transfer.[18] In addition, the introduced NiO phase could function as the buffer layer to accommodate the volume expansion and effectively maintain the structural integrity and stability. In the selected area electron diffraction (SAED) pattern of the NNMO (Figure 3f), the diffraction rings can be assigned to the (111), (200), (220), and (222) planes of NiO phase, as well as to the (220) planes of β-$NiMoO_4$, respectively, which also indicates the coexistence of the two phases in the NNMO composite. This novel architecture and its composition were further researched by the corresponding energy dispersive X-ray spectroscopy (EDX) elemental mapping images (Figure 3g-3j), which confirm the presence of Ni, Mo, and O elements in the NNMO. Moreover, the Ni, Mo and O elements are homogeneously distributed in the entire microsphere, indicating the intimate contact between the two components and the formation of heterostructures. On the contrary, the SEM images

of the NO (Figure S2a,S2b) show networks constructed from many disordered and aggregated rods. The length of the rods is between one and tens of micrometers. Figure S2c,S2d further reveal the general microsphere architecture of α-phase $NiMoO_4$ with several micrometers in average diameters. Although the morphology of α-phase and β-phase $NiMoO_4$ are quite similar, without the introduced NiO phase, the nanosheets of NMO microsphere aggregated severely, resulting in less pores and inferior structural stability.

To further investigate the electrochemical behavior of the synthesized materials for Li-ion batteries, cyclic voltammetry (CV) measurements were conducted. Figure 4a shows the first five consecutive CV curves of NNMO electrode recorded at a scan rate of 0.1 mV/s in the potential range of 0.01–3.00 V versus Li/Li^+. It is evidently observed that from the second to fifth cycles, these CV profiles overlap well, implying the good reversibility and cycling stability of the NNMO electrode during electrochemical reactions. In the first cycle, two intense reduction peaks in the cathodic scan occurred at around 0.59 V and 0.42 V, corresponding to the initial reduction of β-$NiMoO_4$ to Ni and Mo ($NiMoO_4 + 8Li^+ + 8e^- \rightarrow Ni + Mo + 4Li_2O$) and NiO to Ni ($NiO + 2Li^+ + 2e^- \rightarrow Ni + Li_2O$), combined with the formation of amorphous Li_2O and SEI layers.[16,36,37] Meanwhile, the broad peaks in the voltage range from 1.4 V to 1.8 V can be further ascribed to the oxidation process of Mo to Mo^{6+} ($Mo + 3Li_2O \rightarrow MoO_3 + 6Li^+ + 6e^-$),[38] whereas the oxidation of metallic Ni to NiO_x contributes to the anodic peak located at approximately 1.83 V.[39] In the following cycles, the different reduction/oxidation peak pairs of 0.75/1.45 V and

1.42/1.79 V are reversible because of the lithium insertion/extraction process with MoO_3.[39,40] Notably, an anodic peak near 2.25 V is observed in the NNMO electrode, owing to the conversion reaction of Ni to NiO ($Ni + Li_2O \rightarrow NiO + 2Li^+ + 2e^-$).[36] On the other hand, the CV curves of NO and NMO electrodes show different behavior in comparison with that of the NNMO. In the first cathodic process of NO electrode, two sharp peaks are clearly observed at 0.437 V and 0.398 V, respectively, because of the reduction reactions of NiO and the formation of amorphous Li_2O, as well as a partially irreversible SEI layer. The oxidation of metallic Ni to NiO contributes to the anodic peak located at approximately 2.26 V, whereas the anodic peaks located at about 1.805 V are attributed to the formation of Mo. (Figures S3).

Figure 4b shows the typical galvanostatic discharge/charge voltage profiles of NNMO anode from 0.01 to 3.0 V at a current density of 0.2 A g^{-1}. In the first cycle, the NNMO electrode delivered an initial discharge capacity of 1538 mA h g^{-1} and charge capacity of 1282 mA h g^{-1}, corresponding to an initial coulombic efficiency (ICE) of 83%, which is higher than those of the NO (80%) and NMO electrodes (78%) (Figure S4), demonstrating the high reversibility and good stability of the NNMO electrode during the electrochemical reactions. The higher reversible capacity of the NNMO can be explained by the further delithiation reaction observed above 2.0 V (Figure 4a), which is attributed to the catalytic behavior of the metallic nickel nanocrystals and its unique porous hierarchical structure that can shorten ion diffusion pathways.[41] Furthermore, the NNMO anode exhibited excellent cycling stability. As shown in Figure 4c, the NNMO electrode delivered an initial reversible capacity of

1282 mA h g^{-1}, which then gradually increased to 1314 mA h g^{-1}, with the coulombic efficiency nearly 100% after 100 cycles. The feature of increased capacity after the initial cycle is not surprising for a metal oxide-based material, as it always ascribed to the reversible growth of polymeric gel-like layers and capacitive interface storage including electric double layer capacitance, as well as an activation process in the nanostructures.[37] On the contrary, rapid capacity fading and inferior capacity retention are clearly observed in the NO and NMO materials. The high electrochemical reversibility and good cycling stability of the NNMO material may be attributed to the following factors: 1) the *in-situ* generated Ni nanocrystals from the NiO phase could function as a direct catalyst for the reversible decomposition of intermediate Li_2O and the oxidation of metallic Ni and Mo from β-$NiMoO_4$; 2) the NiO nanosheets can act as the mechanical buffer to effectively stabilize the $NiMoO_4$ phase, thus reducing the self-agglomeration of $NiMoO_4$ nanosheets and maintaining good structural stability; 3) the unique hierarchical porous architecture constructed from the small nanosheets will provide more active sites for Li^+ storage, short ion diffusion pathways, as well as abundant additional space to release the internal stress induced by volume changes during discharge/charge process.

Additionally, the NNMO electrode also exhibited remarkable rate capability at different current densities. As can be seen from Figure 4d, the NNMO electrode is capable of delivering the specific capacities of 1360, 1003, 631, 469, and 308 mA h g^{-1} at the current densities of 0.2, 0.5, 1.0, 3.0, and 5.0 A g^{-1}, respectively. More importantly, the capacity can recover to the initial value (about 1339 mA h g^{-1}) when

the current rate is set back to 0.2 A g^{-1} after 60 cycles, indicating the excellent rate capability and good reversibility of the NNMO electrode. On the contrary, both the NO and the NMO electrodes show much inferior capacity retention and severe capacity decay between the current densities of 1 and 5 A g^{-1}. The excellent rate capability can be attributed to the synergistic effects of the binary composition and the short lithium diffusion distance in the porous hierarchical NNMO heterostructure. The long cycling performance is also an important parameter of batteries in practical applications. Hence, we further examined the long-term cycling property of the NNMO electrode at a high current density of 1 A g^{-1} (Figure 4e). After 400 cycles, the NNMO anode still retained a high reversible capacity around 500 mA h g^{-1}, and the average coulombic efficiency is close to 100%. More importantly, the NNMO electrode can maintain the hierarchical porous structure after long-term cycles, demonstrating its good structural stability. The superior structural characteristics, such as the 2D building blocks, large surface area and abundant pores enable its good structural integrity (Figure S5).

To reveal the boosted charge transfer behavior in the NNMO heterostructure, the kinetic differences of lithium ion diffusion in these anodes have been investigated as well. As shown in Figure 5a and 5b, the NNMO sample exhibits larger peak intensities and smaller polarization at all scan rates, indicating the greatly enhanced electrochemical kinetics in the NNMO electrode, which are favorable for achieving better rate capability. Furthermore, the significantly promoted charge transfer process in the NNMO heterostructure also can be proved by the higher diffusion coefficient of

Li^+ compared to the NMO sample (Figure 5c). Meanwhile, the electrochemical impedance spectroscopy (EIS) measurements have been conducted to research the kinetic differences between various electrodes (Figure S6). It is noticed that the diameter of the semicircle in the high–medium–frequency region for the NNMO electrode is much smaller than for the NMO and NO electrodes, demonstrating the highly improved electron/ion transport dynamic in the heterostructure of the NNMO sample.[42,43]

Conclusion

In summary, we have developed a facile strategy to synthesize the novel hierarchical porous NiO/β-$NiMoO_4$ heterostructure constructed from small nanosheets, featuring in large surface area, short ions diffusion paths, and good structural stability. By means of synergistically active ternary metal oxides, boosted charge transfer dynamic, and enhanced electrochemical reversibility, the NNMO heterostructure achieved high reversible capacity, good rate capability and superior long-term cyclability for Li-ion batteries. Our material design strategy presented here could be a promising approach for designing novel heterostructure nanomaterials for high-performance rechargeable batteries.

Experiment Section

Synthesis of hierarchical porous NiO/β-$NiMoO_4$ heterostructure

In a typical synthesis process, 2 mmol nickel acetate tetrahydrate (0.4978 g) and 1

mmol sodium molybdate dehydrate (0.3629 g) with a Ni/Mo molar ratio of 2:1 were slowly added into 30 mL deionized water under magnetic stirring for 30 min to form a transparent solution. The above resultant solution was then transferred to a 50 mL Teflon-lined autoclave, and then it was kept in an oven at 180 °C for 12 h. After the hydrothermal reaction, the obtained green product was separated by centrifugation and washed several times with de-ionized water and ethanol. The resultant composite was then dried at 80 °C overnight, followed by heating in a tube furnace under oxygen atmosphere at 550 °C for 2 h with a ramp rate of 2 °C min^{-1}, yielding the hierarchical NNMO electrode with a Ni : Mo ratio of 2.3:1, as determined by inductively coupled plasma (ICP) (Table S1).

Synthesis of single-phase NiO (NO) materials

The synthesis process is similar to that for NNMO. First, 1.2 mmol nickel chloride hexahydrate (0.2852 g), 3 mmol urea (0.1802 g), and 0.33 mmol cetyltrimethyl ammonium bromide (CTAB, 0.12 g) were added into 30 ml deionized water under magnetic stirring for 30 minutes to form a transparent solution. Then, the above solution was transferred to a 50 mL Teflon-lined autoclave and kept in an oven at 180 °C for 12 h. The obtained slurry was centrifuged, washed with deionized water, and then dried at 80 °C for 24 h. After thermal oxidation at 550 °C for 2 h with a ramp rate of 2 °C min^{-1}, the single phase NiO material was obtained.

Synthesis of single-phase α-$NiMoO_4$ (NMO) materials

In a typical procedure, 1.3 mmol nickel chloride hexahydrate (0.3090 g) and 1.3

mmol sodium molybdate dehydrate (0.3527 g) with a Ni/Mo molar ratio of 1:1 were added into a given amount (30 mL) of distilled water. The resulting solution was then transferred into a Teflon-lined stainless-steel autoclave and maintained at 180 °C for 12 h. After cooling to room temperature, the slurry was washed several times with deionized water and dried at 80 °C for 24 h in an oven. Finally, the dried material, which had a green color, was thermally treated at 550 °C for 2 h in a tube furnace under oxygen atmosphere to yield the α-$NiMoO_4$.

Material characterization

The crystalline structure of the materials was investigated by X-ray diffraction (XRD，Bruker AXS, D8 diffractometer) with Cu Kα radiation at a scanning rate of 1° min^{-1}. The morphology and energy dispersive spectroscopy (EDS) mapping of the as-prepared products were observed by scanning electron microscopy (SEM; JEOL JSM, 6510V), and the details of the crystal structure were further examined by transmission electron microscopy (TEM; FEI TF20). X-ray photoelectron spectroscopy (XPS) was then conducted on an ESCALAB 250XI photoelectron spectrometer using monochromatic Al Kα radiation under vacuum at 2×10^{-6} Pa. All of the binding energies are referenced to the C 1s peak at 284.8 eV of the surface adventitious carbon. The actual contents of the Ni and Mo elements were measured by inductively coupled plasma (ICP) emission spectroscopy using a Perkin Elmer Optimal 8000 instrument (detection limit: 0.01 ppm for Ni, 0.01 ppm for Mo). Specific surface areas and pore size distributions were also obtained from N_2

adsorption/desorption isotherms recorded at 77 K with a Micromeritics ASAP 2020 porosimeter. Prior to surface area measurements, the sample was dried under vacuum at 393 K for 8 h. The surface area was computed using the Brunauer–Emmett–Teller (BET) method, whereas the pore size distribution was calculated in accordance with the Barrett–Joyner–Halenda (BJH) method.

Electrochemical measurements

Electrochemical tests were further conducted on CR 2025 coin-type cells that were assembled in an argon-filled glove box. The working electrodes were prepared by mixing the active materials, Super P, and Na-carboxymethyl cellulose (CMC) in a weight ratio of 60:30:10 then pasted on Cu foil and dried at 80 °C for 12 h in a vacuum oven, which was followed by pressing at 300 kg/cm^2. The mass loading of the materials on individual electrodes was about 1.15 mg cm^{-2}. Electrochemical measurements were further carried out using two-electrode coin cells with Li metal as the counter and reference electrode and Celgard (product 2300) film as the separator. The electrolyte consisted of a solution of 1 M $LiPF_6$ in ethylene carbonate/diethyl carbonate/ethyl methyl carbonate (1:1:1; v/v/v). Electrochemical impedance spectroscopy and cyclic voltammetry were conducted on a CHI 660E electrochemical workstation at different scan rates. The cells were galvanostatically charged/discharged in the voltage range of 0.01–3.00 V versus Li/Li$^+$ at different current densities on a Land CT2001A battery tester.

The lithium-ion diffusion coefficient (D_{Li+}) was further calculated based on the

Randles-Sevcik Equation, as in previously reported methods:[3]

$$i_p = (2.69 \times 10^5)\, n^{3/2}\, SD^{1/2} C v^{1/2} \quad (1)$$

Where i_p is the peak current (A), n is the number of transferred electrons, D_{Li+} is the diffusion coefficient of Li ions ($cm^2\ s^{-1}$), S is the electrode surface area (S = 70.85 mm^2), C is the concentration of Li^+ in the electrolyte, and v is the potential scan rate ($V\ s^{-1}$). Since the electrodes were prepared and tested by the same procedure, the Randles-Sevchik equation can be further simplified as follows:

$$i_p = AD^{1/2}\, v^{1/2} \quad (2)$$

Where A is supposed to be a constant and $AD^{1/2}$ is defined as the apparent diffusion coefficient of Li^+ in the coin cells, which can be calculated by fitting the linear curves.

Acknowledgments

Z. Wang and S. Zhang contributed equally to this work. Financial support provided by the grant from the National Natural Science Foundation of China (No. 21476063) and the Hubei Provincial Natural Science Foundation of China (2018CFB237) is gratefully acknowledged. The authors also thank Dr. T. Silver for critical reading of the manuscript.

Conflict of interest

The authors declare no conflict of interest.

References

[1] J. Mao, T. Zhou, Y. Zheng, H. Gao, H. Liu, Z. Guo, *J. Mater. Chem. A,* **2018**, *6*,

3284–3303.

[2] T. Zhou, Y. Zheng, H. Gao, S. Min, S. Li, H. Liu, Z. Guo, *Adv. Sci.*, **2015**, *2*, 1500027.

[3] J. Yang, Y. Wang, W. Li, L. Wang, Y. Fan, W. Jiang, W. Luo, Y. Wang, B. Kong, C. Selomulya, H. Liu, S. Dou, D. Zhao, *Adv. Mater.*, **2017**, *29*, 1700523.

[4] Y. Liu, T. Zhou, Y. Zheng, Z. He, C. Xiao, W. Pang, W. Tong, Y. Zou, B. Pan, Z. Guo, Y. Xie, *ACS Nano*, **2017**, *11*, 8519–8526.

[5] Y. Zheng, T. Zhou, X. Zhao, W. Pang, H. Gao, S. Li, Z. Zhou, H. Liu, Z. Guo, *Adv. Mater.*, **2017**, *29*, 1700396.

[6] G. Zhang and X. Lou, *Angew. Chem. Int. Ed.*, **2014**, 53, 9041–9044.

[7] C. Tan, Z. Lai, H. Zhang, *Adv. Mater.*, **2017**, *29*, 1701392.

[8] C. Yuan, H. Wu, Y. Xie, X. Lou, *Angew. Chem. Int. Ed.*, **2014**, *53*, 1488–1504.

[9] Y. Zhao, X. Li, B. Yan, D. Xiong, D. Li , S. Lawes, X. Sun, *Adv. Energy Mater.*, **2016**, *6*, 1502175.

[10] Y. Ma, C. Tai, R. Younesi, T. Gustafsson, J. Lee, K. Edström, *Chem. Mater.*, **2015**, *27*, 7698−7709.

[11] T. Wei, C. Chen, H. Chien, S. Lu, C. Hu, *Adv. Mater.*, **2010**, *22*, 347−351.

[12] B. Moreno, E. Chinarro, M. Colomer, J. Jurado, *J. Phys. Chem. C*, **2010**, *114*, 4251−4257.

[13] S. Ratha, A. Samantara, K. Singha, A. Gangan, B. Chakraborty, B. Jena, C. Rout, *ACS Appl. Mater. Interfaces*, **2017**, *9*, 9640−9653.

[14] D. Cai, D. Wang, B.Liu, Y. Wang, Y. Liu, L. Wang, H. Li, H. Huang, Q. Li, T.

Wang, *ACS Appl. Mater. Interfaces,* **2013**, *5*, 12905-12910.

[15] X. Tian, X. Li, T. Yang, K. Wang, H. Wang, Y. Song, Z. Liu, Q. Guo, *Appl. Surf. Sci.*, **2018**, *434*, 49–56.

[16] J. Haetge, I. Djerdj, T. Brezesinski, *Chem. Commun.*, **2012**, *48*, 6726–6728.

[17] M. Cao, Y. Bu, X. Lv, X. Jiang, L. Wang, S. Dai, M. Wang, Y. Shen, *Appl. Surf. Sci.* **2018,** *435*, 641–648.

[18] Y. Zheng, T. Zhou, C. Zhang, J. Mao, H. Liu, Z. Guo, *Angew. Chem. Int. Ed.*, **2016**, *55*, 3408−3413.

[19] E. Pomerantseva1, Y. Gogotsi, *Nat. Energy,* **2017**, *2*, 17089.

[20] L. Hou , L. Lian , L. Zhang , G. Pang , C. Yuan , X. Zhang, *Adv. Funct. Mater*., **2015**, *25*, 238–246.

[21] L. Mai, F. Yang, Y. Zhao, X. Xu, L. Xu, Y. Luo, *Nat. Commun.*, **2011**, *2*, 381−385.

[22] Z. Sun, W. Ai, J.Liu, X. Qi, Y. Wang, J. Zhu, H. Zhang, T. Yu, *Nanoscale,* **2014**, *6*, 6563−6568.

[23] Y. Zhang, Q. Zhuo, X. Lv, Y. Ma, J. Zhong, X. Sun, *Electrochim. Acta*, **2015**, *178*, 590−596.

[24] M. Li,; Y. Yin, C. Li, F. Zhang, L. Wan, S. Xu, D. Evans, *Chem. Commun.*, **2012**, *48*, 410−412.

[25] Y. Chen, Y. Wang, X. Shen, R. Cai, H. Yang, K. Xu, A. Yuan, Z. Ji, *J. Mater. Chem. A*, **2018**. *6*, 1048−1056.

[26] L. Cong, H. Xie, J. Li, *Adv. Energy Mater*., **2017**, 1601906.

[27] Y. Guo, L. Yu, C. Wang, Z. Lin, X. Lou, *Adv. Funct. Mater.*, **2015**, *25*, 5184–5189.

[28] W. Liu, T. Zhou, Y. Zheng, J. Liu, C. Feng, Y. Shen, Y. Huang, Z. Guo, *ACS Appl. Mater. Interfaces*, **2017**, *9*, 9778–9784.

[29] W. Xiao, J. Chen, C. Li, R. Xu, X. Lou, *Chem. Mater.*, **2009**, *22*, 746−754.

[30] S. Zhang, F. Yao, L. Yang, F. Zhang, S. Xu, *Carbon*, **2015**, *93*, 143−150.

[31] A. Vu, Y. Qian, A. Stein, *Adv. Energy Mater.*, **2012**, *2*, 1056−1085.

[32] K. Xiao, L. Xia, G. Liu, S. Wang, L. Ding, H. Wang, *J. Mater. Chem. A*, **2015**, *3*, 6128−6135.

[33] B. Wang, S. Li, X. Wu, J. Liu, W. Tian, *Phys. Chem. Chem. Phys.*, **2016**, *18*, 908−915.

[34] J. Yan, Z. Fan, W. Sun, G. Ning, T. Wei, Q. Zhang, R. Zhang, L. Zhi, F. Wei, *Adv. Funct. Mater.*, **2012**, *22*, 2632−2641.

[35] B. Wang, S. Li, X. Wu, W. Tian, J. Liu, M. Yu, *J. Mater. Chem. A*, **2015**, *3*, 13691−13698.

[36] C. Kim, J. Jung, K. Yoon, D. Youn, S. Park, I. Kim, *ACS Nano*, **2016**, *10*, 11317−11326.

[37] X. Sun, W. Si, X. Liu, J. Deng, L. Xi, L. Liu, C. Yan, O. Schmidt, *Nano Energy*, **2014**, *9*, 168−171.

[38] X. Zhang, X. Song, S. Gao, Y. Xu, X. Cheng, H. Zhao, L. Huo, *J. Mater. Chem. A*, **2013**, *1*, 6858−6864.

[39] J. Ahn, G. Park, Y. Kang, J. Lee, *Electrochim. Acta*, **2015**, *174*, 102−110.

[40] G. Zhao, N. Zhang, K. Sun, *J. Mater. Chem. A*, **2013**, *1*, 221−224.

[41] C. Hua, X. Fang, Z. Wang, L. Chen, *Chem. Eur. J.*, **2014**, *20*, 5487−5491.

[42] K. Cao, L. Jiao, H. Liu, Y. Liu, Y. Wang, Z. Guo, H. Yuan, *Adv. Energy Mater.*, **2015**, *5*, 1401421.

[43] T. Zhou, W. Pang, C. Zhang, J. Yang, Z. Chen, H. Liu, Z. Guo, *ACS Nano*, **2014**, *8*, 8323−8333.

10.1002/cplu.201800220

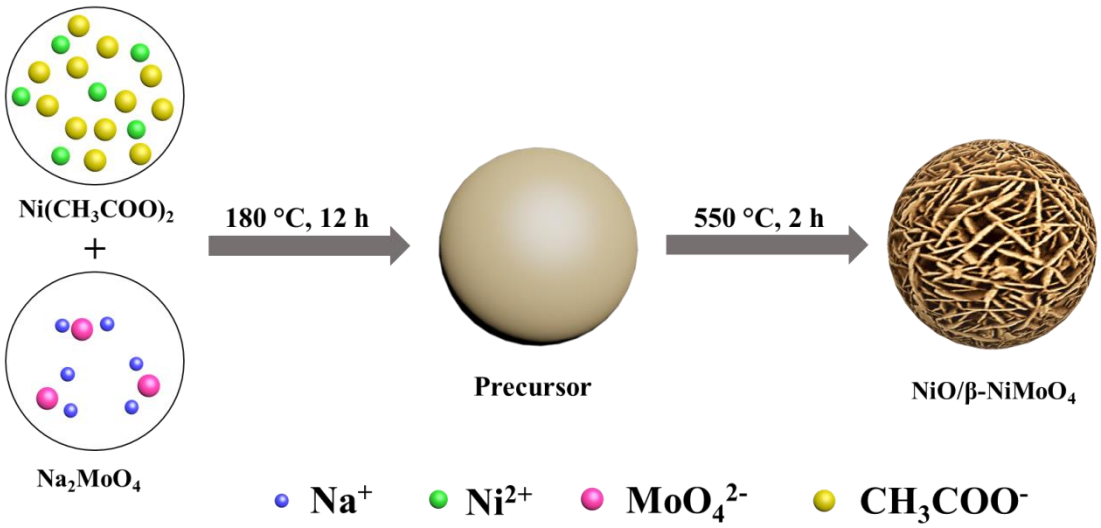

Scheme 1. Schematic illustration of the novel hierarchical porous NiO/β-$NiMoO_4$ (NNMO) heterostructure prepared via a facile hydrothermal method followed by a calcination process.

10.1002/cplu.201800220

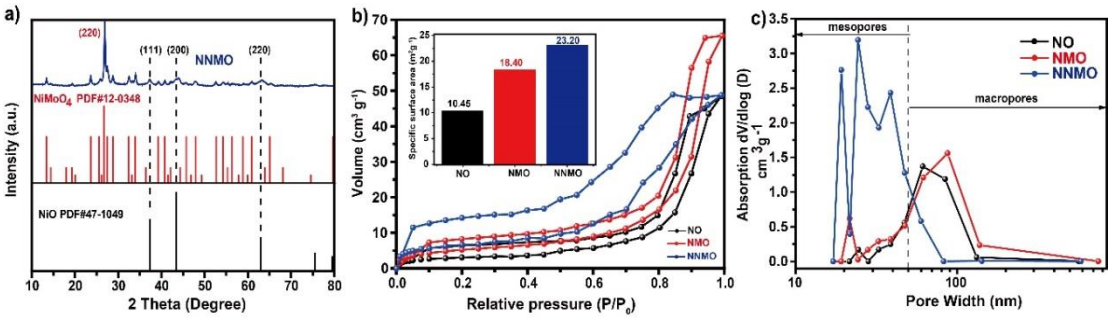

Figure 1. (a) General XRD pattern of as-prepared NNMO; (b) N_2 adsorption/desorption isotherms (inset: comparison of the specific surface areas of NO, NMO, and NNMO) and (d) pore size distributions of those three samples.

10.1002/cplu.201800220

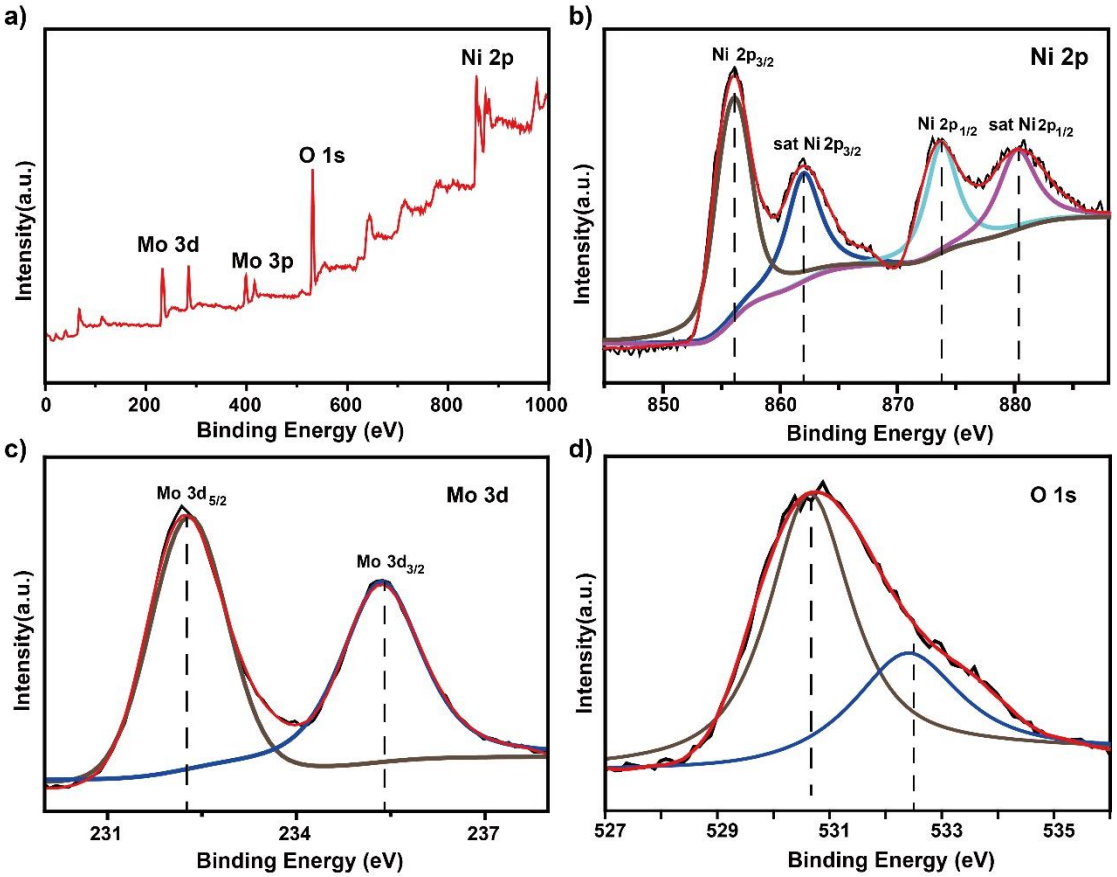

Figure 2. (a) XPS survey spectrum, (b) high resolution Ni 2p spectrum, (c) Mo 3d spectrum, and (d) O 1s region of the obtained NNMO material.

10.1002/cplu.201800220

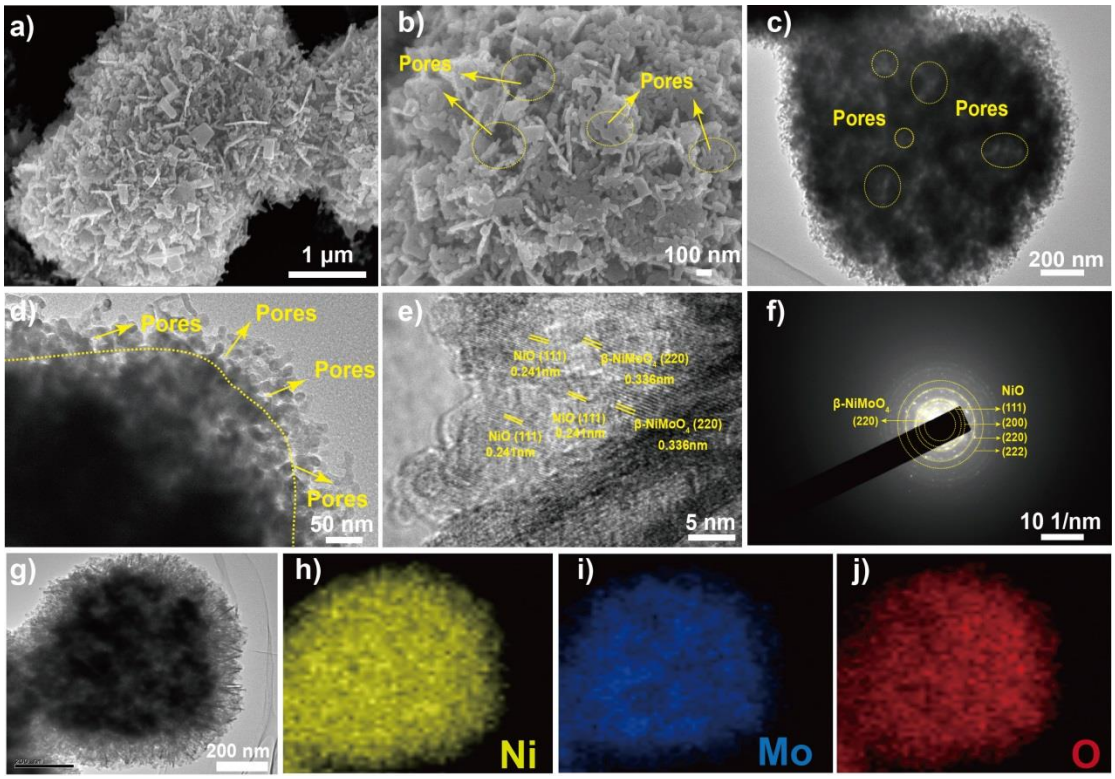

Figure 3. (a,b) Representative SEM images at different magnifications of NNMO; (c–e) TEM and HRTEM images of as-prepared NNMO; (f) SAED pattern and (g–j) Corresponding EDS elemental mapping images of the NNMO material.

10.1002/cplu.201800220

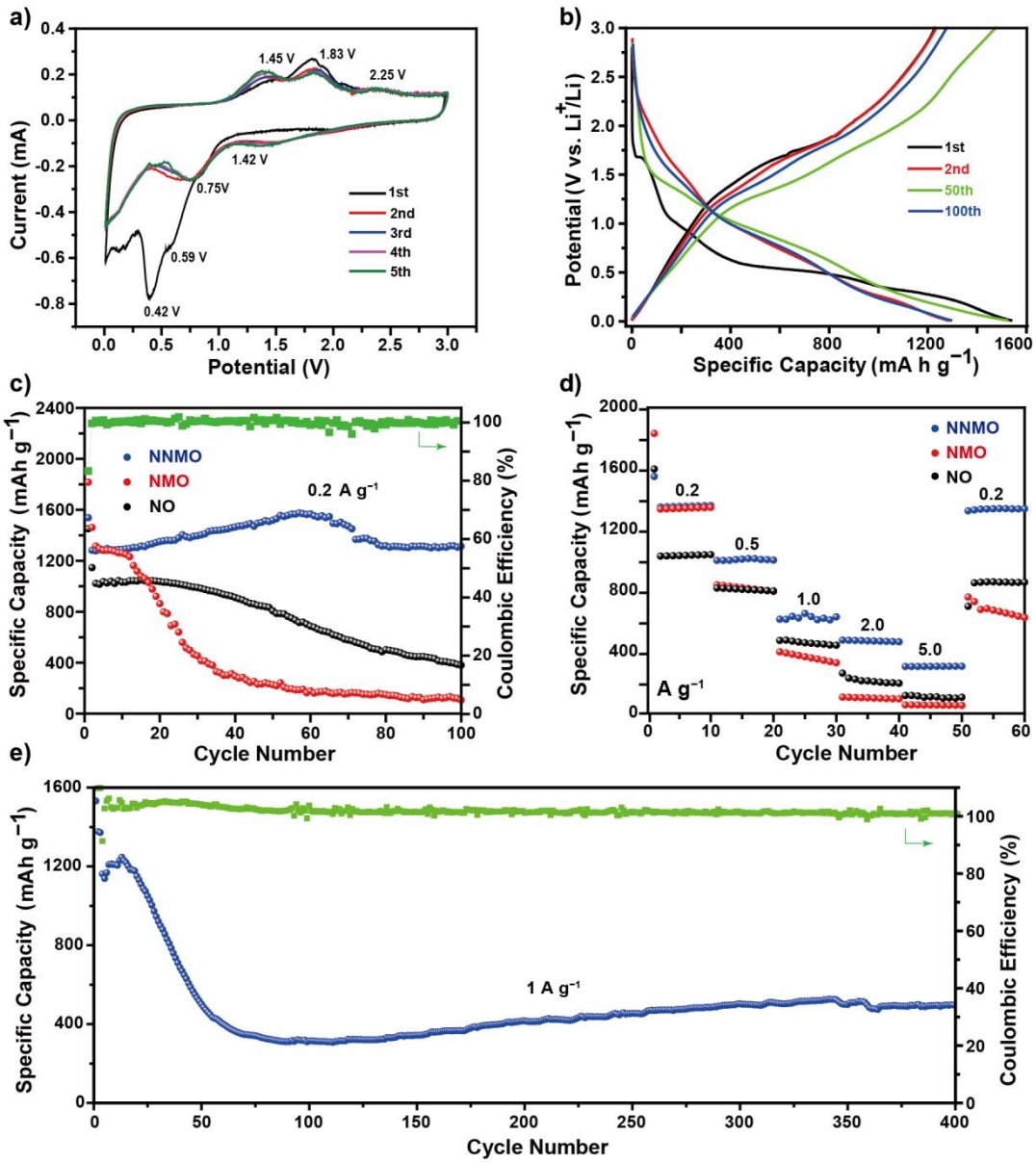

Figure 4. Electrochemical evaluation of NNMO, showing (a) cyclic voltammograms for the first 5 cycles from 0.01 V to 3.00 V; (b) galvanostatic charge/discharge voltage profiles versus capacity of NNMO electrode from for selected cycles at a current rate of 0.2 A g^{-1}; (c) cycling performances of the obtained NO, NMO, and NNMO electrodes at 0.2 A g^{-1} and coulombic efficiency of the NNMO electrode at 0.2 A g^{-1}; (d) rate performances of those three electrodes at varying current rates of 0.2, 0.5, 1, 2, 5, and 0.2 A g^{-1}; (e) long-term cycling performance at 1 A g^{-1} of the obtained NNMO electrode and the corresponding coulombic efficiency.

10.1002/cplu.201800220

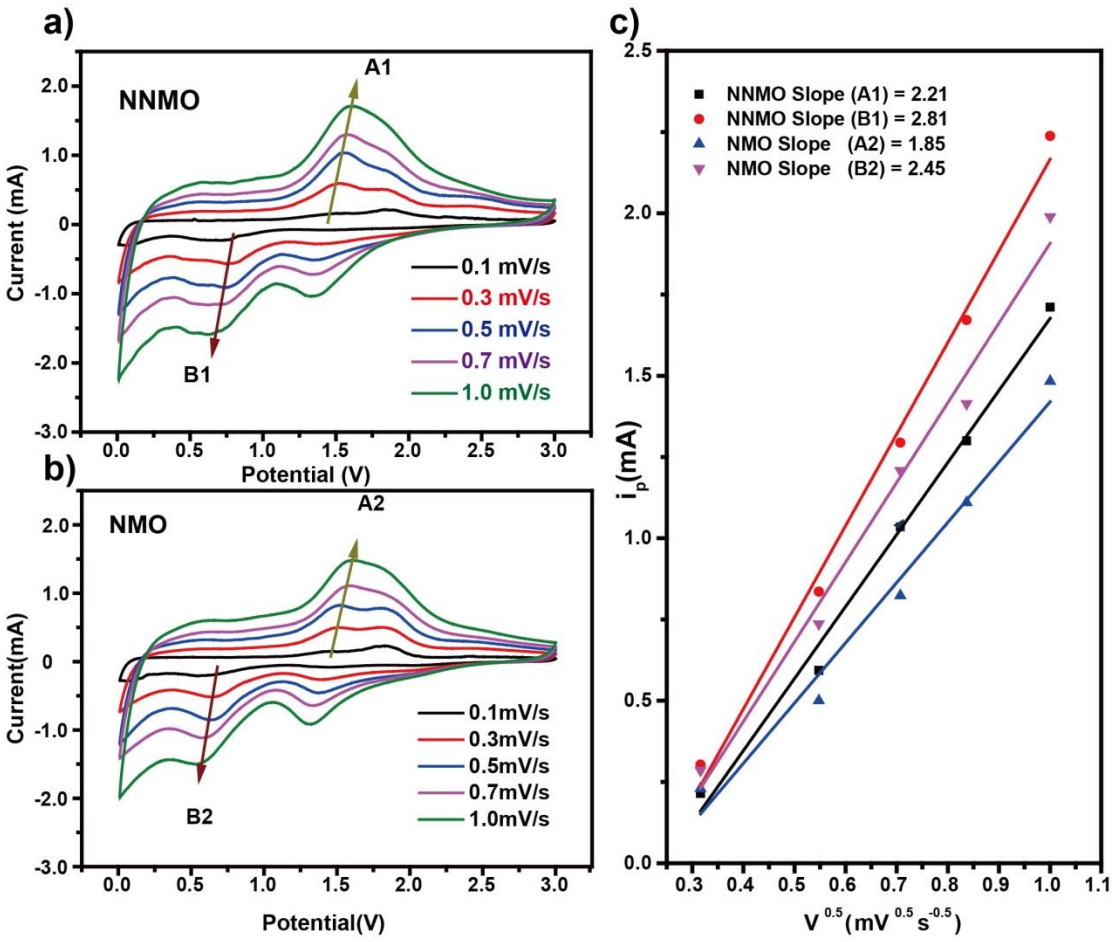

Figure 5. CV curves at different scan rates for LIB cells with (a) NNMO and (b) NMO materials, and (c) the linear relationship between the peak current (i_p) and the square root of the scan rate ($v^{1/2}$) for NNMO electrode.